

## RESEARCH ARTICLE

10.1002/2016JB013102

## Key Points:

- Shear deformation triggers fluid-rock interaction and localized fluid migration
- Coupled and decoupled fracturing modes exist in the subduction interface
- Tensile strength controls the fracturing modes

## Correspondence to:

L. Zheng,  
liangzh.cug@gmail.com

## Citation:

Zheng, L., D. May, T. Gerya, and M. Bostock (2016), Fluid-assisted deformation of the subduction interface: Coupled and decoupled regimes from 2-D hydromechanical modeling, *J. Geophys. Res. Solid Earth*, 121, 6132–6149, doi:10.1002/2016JB013102.

Received 16 APR 2016

Accepted 18 JUL 2016

Accepted article online 20 JUL 2016

Published online 12 AUG 2016

# Fluid-assisted deformation of the subduction interface: Coupled and decoupled regimes from 2-D hydromechanical modeling

Liang Zheng<sup>1</sup>, Dave May<sup>1</sup>, Taras Gerya<sup>1</sup>, and Michael Bostock<sup>2</sup>
<sup>1</sup>Institute of Geophysics, Swiss Federal Institute of Technology (ETH Zurich), Zurich, Switzerland, <sup>2</sup>Department of Earth and Ocean Sciences, University of British Columbia, Vancouver, British Columbia, Canada

**Abstract** Shear deformation, accompanied with fluid activity inside the subduction interface, is related to many tectonic energy-releasing events, including regular and slow earthquakes. We have numerically examined the fluid-rock interactions inside a deforming subduction interface using state-of-the-art 2-D hydromechanical numerical models, which incorporate the rock fracturing behavior as a plastic rheology which is dependent on the pore fluid pressure. Our modeling results suggest that two typical dynamical regimes of the deforming subduction interface exist, namely, a “coupled” and a “decoupled” regime. In the coupled regime the subduction interface is subdivided into multiple rigid blocks, each separated by a narrow shear zone inclined at an angle of 15–20° with respect to the slab surface. In contrast, in the decoupled regime the subduction interface is divided into two distinct layers moving relative to each other along a pervasive slab surface-parallel shear zone. Through a systematic parameter study, we observe that the tensile strength (cohesion) of the material within the subduction interface dictates the resulting style of deformation within the interface: high cohesion (~60 MPa) results in the coupled regime, while low cohesion (~10 MPa) leads to the decoupled regime. We also demonstrate that the lithostatic pressure and inflow/outflow fluid fluxes (i.e., fluid-fluxed boundary condition) influence the location and orientation of faults. Predictions from our numerical models are supported by experimental laboratory studies, geological data, and geophysical observations from modern subduction settings.

## 1. Introduction

The subduction interface is a narrow zone sandwiched between the subducting oceanic slab and the overriding plate. This zone is an area of major tectonic activity where most of the seismic energy is released. A subducting slab will contain a significant volume of water along its upper interface, stored in hydrous minerals or present as a free pore fluid phase [Iwamori and Nakakuki, 2013; Peacock, 1990]. The presence of water along the active plate interface is supported by seismic imaging which indicates a high  $V_p/V_s$  ratio [e.g., Peacock et al., 2011] and high electrical conductivity zones [e.g., Soyer and Unsworth, 2006]. These observations are consistent with laboratory measurements such as the study of the water effects on the Poisson's ratio [Christensen, 1996] and the electrical conductivity of olivine [Wang et al., 2006a].

Increased fluid pressures lower the tensile strength of the material within the interface. Such rheological weakening notably enhances fracturing and faulting in the presence of pressurized percolating aqueous fluid [Cox, 1995; Duarte et al., 2015; Rozhko et al., 2007; Sibson, 1994, 1996; Wang et al., 2006b]. Fluid released by dehydration reactions in the slab is also believed to be an important embrittlement mechanism triggering subduction-related seismicity [e.g., Faccenda et al., 2012; Hacker et al., 2003]. Direct evidence for fluid-induced brittle faulting and fracturing has been established from geological-petrological studies of subduction-related rock complexes, such as the discovery of eclogite-grade hydrothermal vein systems in subducted rocks [Aurthheim, 1987; Sibson and Scott, 1998; Weinberg and Regenauer-Lieb, 2010]. In particular, a recent investigation [Angiboust et al., 2014] demonstrated the interplay between hydrofracturing and eclogite-grade metasomatic processes associated with deep fluid activity within the subduction interface. Moreover, many seismic phenomena within the subduction interface are intrinsically related to the fluid activity, including both regular (“loud”) earthquakes [Shimojo et al., 2014] and slow-slip (“silent”) events, such as episodic tremor and slip (ETS), low-frequency earthquakes, and slow-slip events [see Saffer and Tobin, 2011, and references therein].

In fact, fluid-related faulting/fracturing and seismicity are not limited to the plate interface and can be distributed throughout the entire volume of the subduction system, including both the slab and the

overriding plate [e.g., *Faccenda*, 2014]. Before subduction, oceanic plates are initially hydrated during extension at mid-ocean ridges [e.g., *Ranero et al.*, 2003] and later during bending-related normal faulting in the outer rise regions [e.g., *Faccenda et al.*, 2009; *Grevemeyer et al.*, 2007; *Ranero and Sallares*, 2004], which are observed to be seismically active [e.g., *van Dinther et al.*, 2014, and references therein]. At inter-seismic depths, especially in the region of the overriding plate Moho (~30 km depth), the presence of fluids is generally interpreted as the result of the free pore fluid migrating from the subducted oceanic crust into the overriding lithospheric mantle and thus leading to serpentinization [*Bostock*, 2013]. Such fluid migration, along with the related faulting and fracturing processes, could be responsible for the triggering of slow earthquake events [*Beroza and Ide*, 2011; *Bostock*, 2013; *Gomberg*, 2010]. At intermediate depths (~70–300 km), an updip migration of dehydration-released fluid inside the unbending subducting slab could possibly explain the development of double seismic zones [*Faccenda et al.*, 2009, 2012].

A complete understanding of the diverse relationship between the subduction-related deformation, seismicity, and fluid processes is still lacking. Recently, the application of self-consistent numerical models in which both fluid percolation and rock deformation are intrinsically coupled have been used to investigate this issue [e.g., *Dymkova and Gerya*, 2013; *van Dinther et al.*, 2014]. In the past 20 years, significant progress in numerical modeling of hydration, dehydration, and fluid/melt transport in subduction zones has been made [see *Faccenda*, 2014; *Gerya*, 2011, and references therein]. Many of the state-of-the-art models of subduction incorporate fluid transport through a porous media, melting, melt segregation, and melt extraction. The inclusion of these physical processes has been performed using various approaches including a kinematic prescription [e.g., *Arcay et al.*, 2005; *Gerya et al.*, 2002, 2006, 2008], diffusion flow [e.g., *Richard et al.*, 2006; *Richard and Bercovici*, 2009], diapiric rise [e.g., *Gerya and Yuen*, 2003; *Zhu et al.*, 2009], and pore fluid flow [e.g., *Cagnioncle et al.*, 2007; *Faccenda et al.*, 2009, 2012; *Hebert et al.*, 2009; *Iwamori*, 1998, 2000, 2004, 2007]. The assumptions utilized within the models of fluid transport differ by adopting a simplified kinematic model describing fluid migration [e.g., *Faccenda et al.*, 2009], not considering porosity evolution and assuming a simplified rock rheology [e.g., *Iwamori and Nakakuki*, 2013], excluding porosity and permeability coupling to the fluid/melt percolation process [e.g., *Cagnioncle et al.*, 2007; *Hebert et al.*, 2009], or prescribing a constant porosity and permeability [e.g., *Faccenda et al.*, 2012]. Indeed, there is a recent trend to apply a complete geodynamic two-phase flow theory within fully hydromechanically coupled numerical models using a realistic visco-(elasto)-(plastic) rock rheology [*Dymkova and Gerya*, 2013; *Keller et al.*, 2013; *Wilson et al.*, 2014]. The governing equations for the coupled hydromechanical system were derived in the 1980s [*McKenzie*, 1984; *Stevenson and Scott*, 1991]; however, in the context of subduction modeling, they have not been implemented in their full complexity due to the methodological and hardware limitations. Recent studies from hydromechanically coupled models [*Dymkova and Gerya*, 2013; *Wilson et al.*, 2014] provide a more self-consistent description of fluid and melt migration in subduction zones. However, these models were limited to relatively low spatial resolution, and thus, they do not provide a detailed examination of the fluid-related faulting and fracturing process occurring within the subduction interface.

In this paper, we will use a recently developed coupled hydromechanical poro-visco-plastic modeling approach [*Dymkova and Gerya*, 2013] to study the relationship between the fluid migration and rock deformation within the subduction interface through high-resolution numerical models. The main objective is to analyze the spatial and temporal variations of fluid flow inside the deforming subduction interface and to understand the relationship between fluid migration and the modes of brittle deformation occurring within the interface.

## 2. Governing Equations

Our long-term hydromechanical numerical models of the subduction interface are based on a poro-visco-plastic two-phase flow approach [*Dymkova and Gerya*, 2013], which define the coupling between the bulk rock deformation (solid) and the pore fluid percolation [*Stevenson and Scott*, 1991].

In this study, the media within the subduction interface is represented via two phases: a solid phase and a fluid phase. The solid phase represents the deformable porous rock matrix, and the fluid phase represents the fluid which can migrate within the porous solid matrix. The proportion of each phase is defined by the volume fraction, namely, porosity  $\phi$ , according to

$$\phi = \frac{\phi_f}{\phi_f + \phi_s}, \quad (1)$$

where  $\phi_f$  represents the volume fraction of the fluid phase and  $\phi_s$  represents the volume fraction of the solid phase. Throughout the remainder, the subscripts  $f$  and  $s$  will always be used to denote quantities attributed to the fluid phase or solid phase, respectively. The porosity relates individual fluid, solid quantities to the total (or bulk) quantity. For instance, the bulk density  $\rho$  is related to the fluid density  $\rho_f$  and solid density  $\rho_s$  via

$$\rho = \phi \rho_f + (1 - \phi) \rho_s. \quad (2)$$

Similarly, the bulk (total) pressure  $P$  is related to the fluid pressure  $P_f$  and the solid pressure  $P_s$  via

$$P = \phi P_f + (1 - \phi) P_s. \quad (3)$$

Porosity evolves with time according to the viscous compaction equation [Connolly and Podladchikov, 1998; Fowler, 1990a; Morency et al., 2007] in accordance with the effective pore pressure  $P_{\text{eff}} = P - P_f$  as

$$\frac{D \ln(1 - \phi)}{Dt} = \frac{P - P_f}{\zeta} = \frac{P_{\text{eff}}}{\zeta}, \quad (4)$$

where  $\zeta$  is the bulk viscosity of the solid. The bulk viscosity is parameterized via [Stevenson and Scott, 1991]

$$\zeta = \frac{\eta}{\phi}, \quad (5)$$

where  $\eta$  is the shear viscosity of the solid. Over tectonic time scales, the conservation of momentum of the solid phase can be described by a highly viscous fluid (e.g., stationary Stokes equations), which is written in the solid matrix velocity frame as

$$\nabla \cdot \sigma' - \nabla P + \rho \vec{g} = 0, \quad (6)$$

where  $\vec{g}$  is the gravity vector and  $\sigma'$  is the deviatoric stress tensor for the bulk material (i.e., solid + fluid).

The fluid flow through the solid matrix is described by Darcy's law

$$\vec{v}_f - \vec{v}_s = -\frac{k}{\eta_f \phi} (\nabla P_f - \rho_f \vec{g}), \quad (7)$$

where  $\vec{v}_f$  is the fluid velocity,  $\vec{v}_s$  is the solid velocity,  $k$  is the permeability, and  $\eta_f$  is the fluid viscosity. Here we have used the cubic porosity-permeability relationship [Gueguen and Dienes, 1989]

$$k = k_0 (\phi / \phi_0)^3, \quad (8)$$

where  $k_0$  and  $\phi_0$  define a reference permeability and reference porosity, respectively.

Given the definition of the Darcy velocity (or Darcy flux)

$$\vec{v}_D = \phi (\vec{v}_f - \vec{v}_s), \quad (9)$$

which describes the fluid flux per unit rock volume, the continuity equations for the solid and fluid phases can be expressed as [Fowler, 1990b; McKenzie, 1984; Stevenson and Scott, 1991]

$$\nabla \cdot \vec{v}_s = -\frac{P - P_f}{\zeta}, \quad (10)$$

$$\nabla \cdot \vec{v}_D = \frac{P - P_f}{\zeta}. \quad (11)$$

From the definition of Stokes (equation (6)) and Darcy equation (equation (7)), there are several alternatives to define the two-phase system describing the conservation of mass and momentum for the fluid and solid phases. One could combine Darcy's equation with the continuity equations for both the fluid and solid. For instance, substituting equations (9) and (11) into equation (7) yields

$$\frac{P - P_f}{\zeta} + \nabla \cdot \left( \frac{k}{\eta_f} (\nabla P_f - \rho_f \vec{g}) \right) = 0. \quad (12)$$

Thus, the two-phase system consists of Stokes equation (equation (6)), solid continuity equation (equation (10)), and the hybrid Darcy/fluid continuity equation (equation (12)). This is the approach adopted in Dymkova [2014] and Dymkova and Gerya [2013]. Rather than eliminating the fluid velocity, an alternative

approach is to use the original definition of the Darcy velocity (equation (9)) in the Darcy equation (equation (7)), yielding

$$\vec{v}_D = -\frac{k}{\eta_f} (\nabla P_f - \rho_f \vec{g}). \quad (13)$$

With this choice, the two-phase system consists of Stokes equation (equation (6)), the solid continuity equation (equation (10)), Darcy's equation (equation (13)), and the fluid continuity equation (equation (11)). In this study, we have elected to use the latter approach as it permits the Darcy velocity to be imposed as a boundary condition, which will form part of our parametric study. We note that both formulations are identical with an appropriate choice of boundary conditions.

The deviatoric stress of the bulk material is given by

$$\sigma'_{ij} = 2\eta \dot{\epsilon}'_{ij}, \quad (14)$$

where  $\dot{\epsilon}'_{ij}$  is the deviatoric strain rate tensor. Specially, in our 2-D case, we can link the deviatoric strain rate with the solid velocity components as

$$\dot{\epsilon}'_{xx} = \frac{1}{2} \left( \frac{\partial v_s^x}{\partial x} - \frac{\partial v_s^y}{\partial y} \right), \quad (15)$$

$$\dot{\epsilon}'_{yy} = \frac{1}{2} \left( \frac{\partial v_s^y}{\partial y} - \frac{\partial v_s^x}{\partial x} \right), \quad (16)$$

$$\dot{\epsilon}'_{xy} = \frac{1}{2} \left( \frac{\partial v_s^x}{\partial y} + \frac{\partial v_s^y}{\partial x} \right), \quad (17)$$

where  $\dot{\epsilon}'_{xx}$ ,  $\dot{\epsilon}'_{yy}$ , and  $\dot{\epsilon}'_{xy}$  are the components of deviatoric strain rate tensor and  $v_s^x$  and  $v_s^y$  are the  $x$  and  $y$  components of solid velocity. The Newtonian shear viscosity of the fluid-bearing rock is calculated using an empirical formula [Katz *et al.*, 2006, and references therein]

$$\eta = \eta_0 \exp(-\alpha \phi), \quad (18)$$

in which  $\eta_0$  is the shear viscosity of the solid at reference zero porosity and  $\alpha = 30$ .

Brittle/plastic deformation in the presence of fluid is described by a Drucker-Prager yield criterion which accounts for pore fluid pressure [Ranalli, 1995]

$$\sigma_{\text{yield}} = C + \gamma(P - P_f), \quad (19)$$

where  $\sigma_{\text{yield}}$  defines the maximum yield strength (YS) which the rock can withstand,  $C$  is the tensile strength of rock (cohesion), and  $\gamma$  is defined as

$$\gamma = \begin{cases} 1.0 & \text{when } P_f > P \\ \mu & \text{when } P_f < P \end{cases}, \quad (20)$$

where  $\mu$  is the internal friction coefficient and  $\gamma = 1.0$  indicates the tensile status when the fluid pressure is greater than the total pressure. When the calculated second invariant of the deviatoric stress, which is defined as

$$\sigma_{\parallel} = \sqrt{\frac{1}{2} (\sigma'_{ij})^2}, \quad (21)$$

is greater than the maximum yield strength, the rock is assumed to deform plastically and the shear viscosity of the solid is modified according to

$$\eta = \frac{\sigma_{\text{yield}}}{2\dot{\epsilon}_{\parallel}}, \quad (22)$$

where  $\dot{\epsilon}_{\parallel}$  is the second invariant of the solid deviatoric strain rate tensor  $\dot{\epsilon}'_{ij}$

$$\dot{\epsilon}_{\parallel} = \sqrt{\frac{1}{2} (\dot{\epsilon}'_{ij})^2}. \quad (23)$$

In order to solve the conservation of mass and momentum for the fluid-solid phases in a domain  $\Omega$ , we define (i) velocity Dirichlet boundary conditions

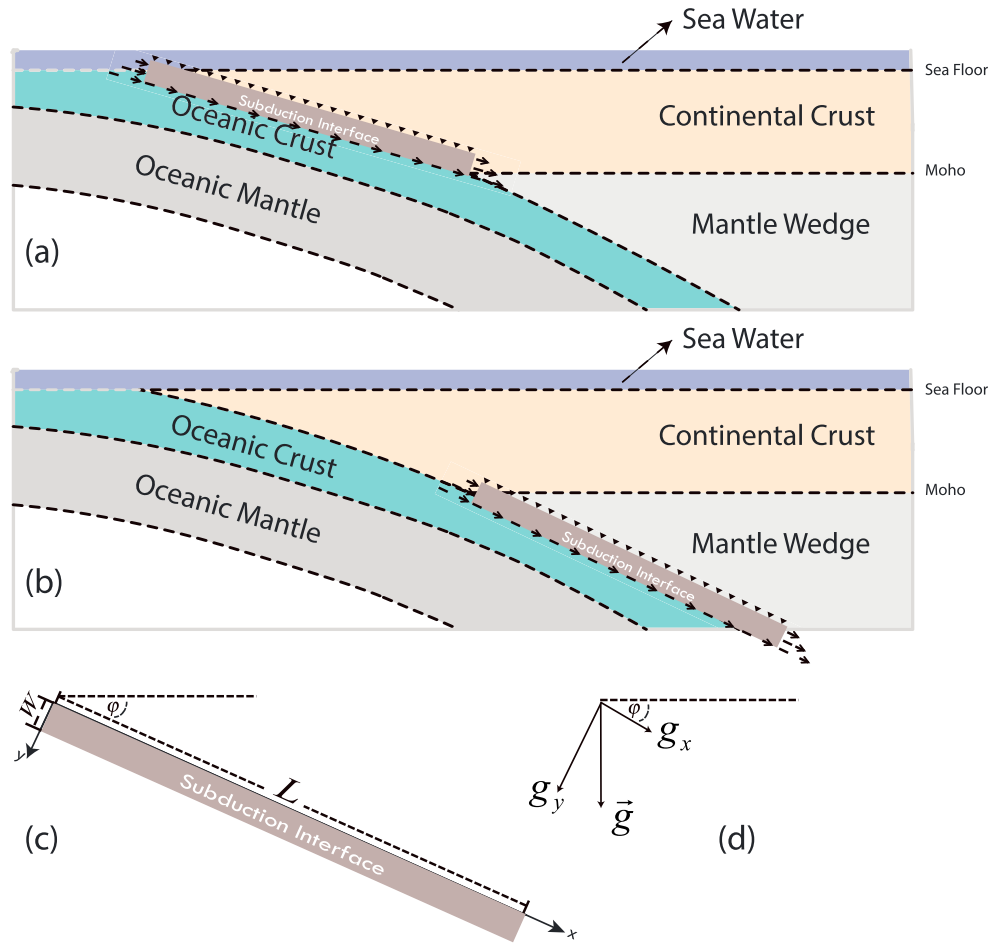


**Figure 1.** Simplified generic subduction interface models (not to scale): (a) subduction interface located between the oceanic crust and continental crust, (b) subduction interface located between the oceanic crust and the mantle wedge, (c) coordinate system, and (d) gravity vector. In Figures 1a and 1b, the model domain is indicated with the dark grey rectangular box. The upper boundary is fixed, and lower boundary moves downward along with the slab. Our model domain approximates the slab interface as planar surface defined with width  $W$  and length  $L$ . The coordinate system is defined in Figure 1c such that the  $x$  axis is parallel to the direction of slab motion with a dip angle  $\phi$ . Accordingly, in Figure 1d, the gravity vector  $\vec{g}$  is decomposed into two nonzero components denoted via  $g_x$  and  $g_y$ .

$$\vec{v}_s|_{\partial\Omega} = \vec{v}_{\text{bond}_s}, \quad (24)$$

$$\vec{v}_D|_{\partial\Omega} = \vec{v}_{\text{bond}_D}, \quad (25)$$

where  $\vec{v}_{\text{bond}_s}$  and  $\vec{v}_{\text{bond}_D}$  are the prescribed solid velocity and Darcy velocity at the boundary of the domain, and (ii) a Dirichlet boundary condition for the total (bulk) pressure  $P$

$$P|_{\partial\Omega} = P_{\text{bond}}, \quad (26)$$

where  $P_{\text{bond}}$  is the prescribed total pressure at the boundary of the domain.

In this work, we solve the two-phase flow equations using a staggered finite difference method combined with the marker-in-cell method based on the methodology introduced in Gerya and Yuen [2003] and further extended for hydromechanical models [Dymkova, 2014; Dymkova and Gerya, 2013].

### 3. Model Setting

The subduction interface is located between the upper oceanic crust and the continental lithosphere/mantle wedge, where hydration and dehydration take place. In Figure 1 we depict the geometry of two segments of subduction interface we have considered. Figure 1a defines a “shallow” subduction segment which starts

**Table 1.** Parameters Used for All Subduction Interface Numerical Experiments

Symbol	Description of the Parameters	Unit	Value(s)
$L$	Length of the subduction interface	km	50.0
$W$	Thickness of the subduction interface	km	2.0
$\phi$	Dip angle of subduction interface	-	30
$\phi_0$	Reference porosity	-	0.01
$\eta_0$	Reference bulk viscosity	Pa s	2.0E20
$k_0$	Reference permeability	m <sup>2</sup>	1.0E-18
$g$	Acceleration of gravity	m/s <sup>2</sup>	9.81
$\mu$	Friction coefficient	-	0.6
$\eta_f$	Fluid shear viscosity	Pa s	1.0E-3
$\rho_f$	Fluid density	kg/m <sup>3</sup>	1000.0
$\rho_s$	Solid density	kg/m <sup>3</sup>	3000.0
$v_{\text{slab}}$	Solid matrix velocity of the slab	cm/yr	5.0
$P_{\text{conf\_air}}$	Confining atmospheric pressure at the Earth's surface (0 km)	MPa	0.1
$P_{\text{conf\_lith}}$	Confining lithostatic pressure at the Moho (30 km)	MPa	1000

from the surface of the Earth and is located between the oceanic crust and continental crust. Figure 1b depicts a “deep” subduction segment which starts from the depth of the Moho (30 km) and is located between the oceanic crust and mantle wedge. The model domain we consider is a rectangular region indicated as “subduction interface” in Figure 1.

Across the model domain, a pure shear velocity boundary condition is prescribed. This is defined by setting the tangential velocity of the solid velocity to zero along the upper boundary and prescribing the tangential velocity of the solid velocity on the lower boundary to be given by the speed of the subducting slab ( $v_{\text{slab}}$ ). Here we consider the speed of subduction to be a constant equal to 5 cm/yr. Along the lateral (left and right) faces of the subduction interface, the horizontal components of solid velocity are defined from the imposed background shear, e.g.,

$$v_{\text{bond}_s}^x|_{y=0} = 0, v_{\text{bond}_s}^x|_{y=W} = v_{\text{slab}}, v_{\text{bond}_s}^x|_{x=0,x=L} = \frac{y}{W} v_{\text{slab}}. \quad (27)$$

Initially, material within the subduction interface is defined to have a reference (initial) porosity of  $\phi_0 = 0.01$  and a reference (initial) bulk shear viscosity  $\eta_0 = 2\text{e}20$  Pa s. The low value of the shear viscosity was chosen to mimic the inherent weakening associated with the initial presence of fluids [Duarte *et al.*, 2015; Gerya *et al.*, 2002; Wada *et al.*, 2008]. During the simulations, we impose limits on the maximum/minimum allowable shear/bulk viscosity and porosity variation according to

$$\eta \in [1.0\text{e}18, 1.0\text{e}22] \text{ Pa s}, \quad (28)$$

$$\zeta \in [1.0\text{e}18, 1.0\text{e}26] \text{ Pa s}, \quad (29)$$

$$\phi \in [1.0\text{e}-6, 1.0]. \quad (30)$$

In all experiments, we use a uniformly spaced finite difference mesh employing a constant spatial resolution in both the  $x$  and  $y$  directions of 100 m. The time step is set as 1000 years at the beginning and then is adjusted according to the maximum velocity of the markers at each time step, so as to avoid markers moving more than a single grid cell in one step.

The parameters associated with geometry of the model, initial conditions, boundary conditions, and rheology are listed in Table 1.

#### 4. Numerical Results

In the following section, we discuss in detail the results of six typical subduction interface models. These models are labeled M1 through to M6 and are summarized in Figure 2. The parameters used for each model are reported in Table 2.



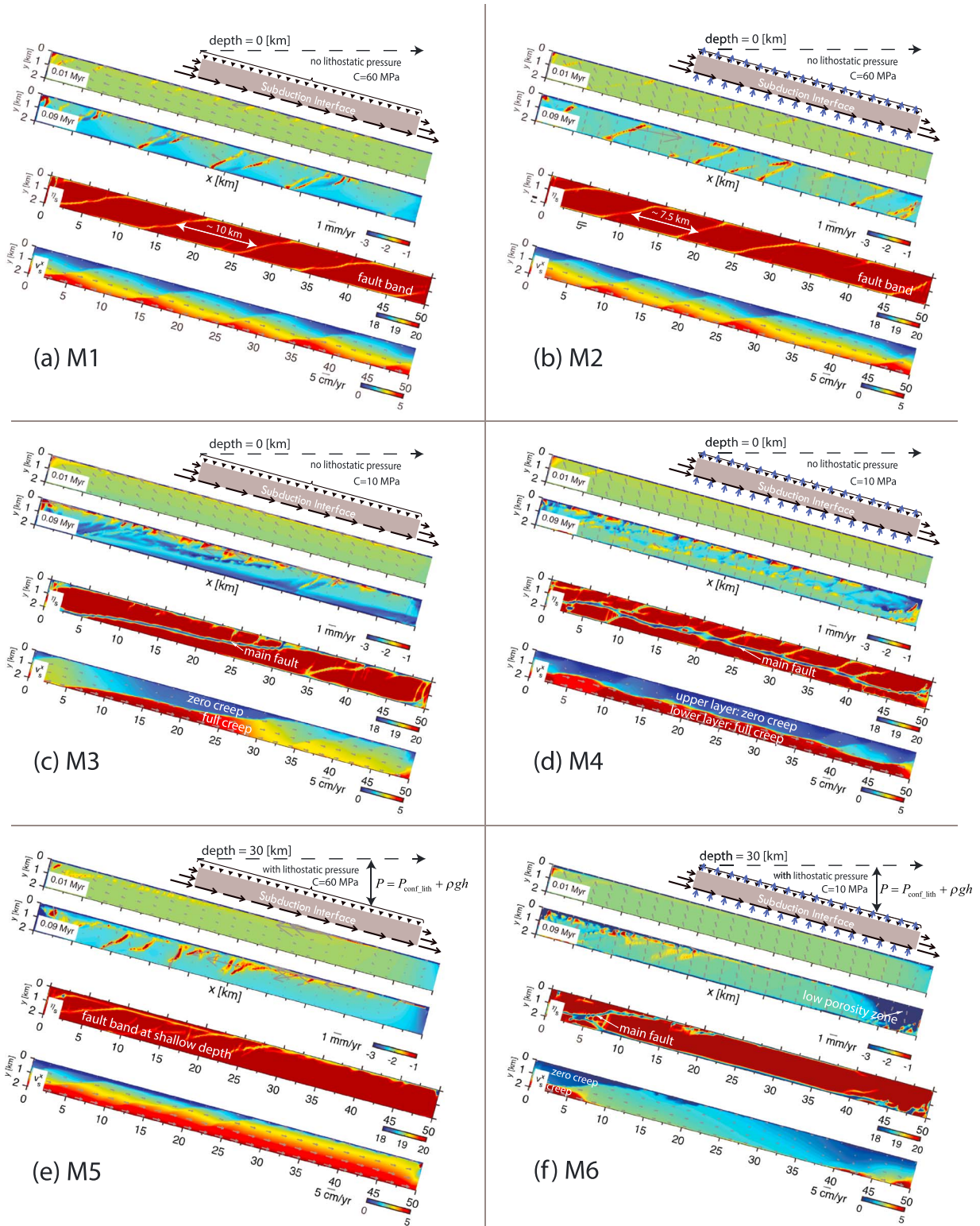


**Figure 2.** (a–f) Typical numerical results of models M1–M6 (see Table 2 for the model specific parameters). Shown within each plot (from top to bottom) are (i) the model type (e.g., shallow and deep) and boundary conditions, (ii) the porosity ( $\log_{10} \phi$ , colors) together with the Darcy velocity ( $\vec{v}_D$ , arrows) at 0.01 Myr, (iii) the porosity ( $\log_{10} \phi$ , colors) together with the Darcy velocity ( $\vec{v}_D$ , arrows) at 0.09 Myr, (iv) the shear viscosity ( $\log_{10} \eta$ , colors) at 0.09 Myr, and (v) the horizontal component of solid velocity ( $v_s^x$ , colors) together with the solid velocity ( $\vec{v}_s$ , arrows) at 0.09 Myr.  $C$  stands for the cohesion;  $P$  and  $P_{\text{conf\_lith}}$  stand for the lithostatic pressure boundary condition and the confining lithostatic pressure at the uppermost part of the model, respectively; and  $\rho$ ,  $g$ , and  $h$  represent the lithospheric density, acceleration of gravity, and depth within the subduction interface, respectively.

**Table 2.** Boundary Conditions and Material Properties for the Reference Models (M1–M6) and for the Parameter Sensitivity Experiments (M7–M12)

Model	$v_D^{\text{inflow}}$ and $v_D^{\text{outflow}}$ (m/s)	$C$ (MPa)	$\mu$	$P_{\text{bond}} _{y=0}$ (MPa)
M1	0	60	0.6	0.1
M2	$1.0\text{E}-11$	60	0.6	0.1
M3	0	10	0.6	0.1
M4	$1.0\text{E}-11$	10	0.6	0.1
M5	0	60	0.6	1000
M6	$1.0\text{E}-11$	10	0.6	1000
M7	$1.0\text{E}-11$	20	0.6	0.1
M8	$1.0\text{E}-11$	30	0.6	0.1
M9	$1.0\text{E}-11$	40	0.6	0.1
M10	$1.0\text{E}-11$	50	0.6	0.1
M11	$1.0\text{E}-11$	60	0.3	0.1
M12	$1.0\text{E}-11$	60	0.1	0.1

#### 4.1. Reference Model

We designed an initial reference model M1 (Table 2 and Figure 2a) with a high rock strength and high tensile strength (here high cohesion is set as  $C = 60$  MPa) without a “fluid-fluxed” boundary condition. The top left corner of the subduction interface M1 is at the Earth’s surface; thus,

$$P_{\text{bond}}|_{x=0,y=0} = P_{\text{conf\_air}}, \quad (31)$$

where  $P_{\text{conf\_air}} = 0.1$  MPa is the confining pressure at the Earth’s surface, e.g., atmospheric pressure.

The results of model M1 (Figure 2a) indicate that fluid migration within the subduction interface is strongly controlled by the plastic deformation of the solid matrix. In this model, fluid flows uniformly toward shallow depths at the beginning of the experiment (0.01 Myr; see porosity plot in Figure 2a). The Darcy velocity decreases with time (see Darcy velocity arrow length at 0.01 Myr and 0.09 Myr in Figure 2a), and the initially uniform fluid migration transitions with the development of multiple fractures (shear zones). These shear zones dip against the motion of the lower plate and are oriented at  $15\text{--}20^\circ$  with respect to the subduction interface (see the viscosity in Figure 2a). These high-porosity and high-permeability structures lead to localized upward fluid movement (see porosity and Darcy velocity in Figure 2a). We note that the location of the high-porosity bands do not always coincide with the shear zones within the subduction interface, because both of the fluid weakening and plastic yielding control the shear band patterns. At 0.09 Myr, the deformation of the solid matrix is partitioned into a collection of coupled, rigid rectangular blocks separated by a narrow shear zones, typified by locally high velocity and low shear viscosity. We refer to this mode of deformation as the “coupled” regime.

#### 4.2. Influence of the Fluid-Fluxed Boundary

In model M2 (Table 2 and Figure 2b), we examine the effect of inflow/outflow fluid-fluxed boundary (implemented by prescribing a constant Darcy velocity). The “washed” subduction interface model was designed to simulate an idealized scenario of mineral dehydration releasing fluids from the oceanic crust into the overriding plate. While fluid-induced rheological weakening may actually lower the tensile strength of rocks, here we used the same high value of cohesion ( $C = 60$  MPa) to isolate the effect of the fluid-fluxed boundary with respect to the reference model M1. Thus, model M2 is identical to model M1 but introduces the fluid-fluxed Darcy velocity boundary as

$$v_{\text{bond\_D}}^y|_{y=0,y=W} = v_D^{\text{inflow}} = v_D^{\text{outflow}}, \quad (32)$$

where the values for inflow/outflow velocity are reported in Table 2 and depicted via blue arrows in Figure 2b.

From Figure 2b, it is clear that the introduction of the fluid-fluxed boundary does not change the characteristics of the coupled regime of the deformation within the subduction interface. Comparison of models M1 and M2 shows that (see Figures 2a and 2b) (1) both models produce noncollocated high-porosity bands and shear bands, (2) imposing the inflow/outflow of the fluid in model M2 adjusts the orientation of fluid path to be oriented more orthogonally toward the top boundary of the subduction interface, and (3) the spacing



between shear bands appears to be reduced in the fluid-fluxed model M2 (~7.5 km) compared to the reference model M1 (~10 km).

### 4.3. Influence of Tensile Strength

According to the definition of the yield stress, tensile strength (cohesion) provides a first-order control on the magnitude of  $\sigma_{\text{yield}}$ . To support this claim, we performed experiments with low tensile strength ( $C = 10$  MPa) with and without the imposed fluid-fluxed boundary condition. These models are defined as M3 and M4, respectively.

In model M3, initially, the direction of fluid migrating is similar to the fluid-fluxed model M2. As in the nonfluid-fluxed model M1, here the Darcy velocity is observed to decrease in magnitude over time. In contrast to model M1, a large coherent low-porosity zone develops along the lower boundary of the subduction interface, along with localized regions of high porosity at the top boundary (see porosity plots at 0.09 Myr in Figures 2a and 2c). Crosscutting the interface is a twisted main shear zone which divides the interface into a stationary rigid upper block and a moving rigid lower block. The crosscutting shear zone is highly oblique and approximately parallel ( $3\text{--}10^\circ$ ) to the boundaries of the subduction interface. We classify the deformation of the solid matrix in this model as the “decoupled” regime.

In model M4 (Figure 2d), a gently curved shear zone with high-porosity patches is generated at the center of the subduction interface over the entire model domain, resulting in a fully decoupled regime.

Comparison of models M3 and M4 indicate that (1) both models lead to the decoupled regimes and (2) when the tensile strength is low, fluid fluxing through the lower boundary precludes the development of a low-porosity zone at the lower boundary and changes the orientation of the main shear zone to be parallel to the subduction interface.

### 4.4. Influence of Imposed Lithostatic Pressure

Models M5 (Figure 2d) and M6 (Figure 2e) consider the effect of lithostatic pressure associated with the buoyancy of the overriding plate. Based on the location of where most slow-slip events have been recorded [Brown *et al.*, 2009], we placed the uppermost part of the subduction interface at the Moho depth of 30 km.

The solid velocity, Darcy velocity boundary conditions, and cohesions for models M5 and M6 are the same as for the reference models M1 and M4, respectively. However, an additional lithostatic pressure boundary condition for models M5 and M6 is defined along the entire upper model boundary as

$$P_{\text{bond}}|_{y=0} = P_{\text{conf\_lith}} + \rho gh = P_{\text{conf\_lith}} + \rho g_x \sin \varphi, \quad (33)$$

where  $P_{\text{conf\_lith}}$  is the confining lithostatic pressure at the uppermost part of the model (refer to Table 2),  $h$  is the depth within the subduction interface,  $x$  is the horizontal position of the subduction interface, and  $\sin \varphi = \frac{h}{x}$ . Due to the unknown porosity of the overriding plate, here we used  $\rho = \rho_s$  as a first-order approximation.

In model M5, the fluid flows uniformly toward the shallow depths within the interface at the beginning of the model (porosity and Darcy velocity field for 0.01 Myr in Figure 2e). At later times (0.09 Myr), the fluid velocity is approximately zero everywhere within the interface, except inside the regions with high porosity. The imposed lithostatic pressure at the base of the model results in larger values of  $(P - P_f)$  at depth, causing a larger yield stress at depth compared to models M1 and M4. As a result, faulting only occurs within the upper part of the model. Fluid activity was observed to concentrate in the newly generated fractures. Compared to model M1, the spacing of shear bands is notably reduced.

In model M6, the inclusion of an inflow/outflow fluid-fluxed boundary condition also modifies the fluid-migrating path such that it is oriented normal with respect to the upper boundary. Analogously to model M5, porosity bands only develop at shallower depths. A low-porosity region develops with time in the deepest part of the model (0.09 Myr; Figure 2f). A short subduction interface-parallel shear zone is generated at shallow depth.

Visually, the faulting pattern of model M5 is analogous to that observed in model M1 but with different faulting positions. A similar conclusion can be made in comparing the shear zones in models M6 with those in model M4. This implies that primary effect of imposing the lithostatic pressure is to move the depth where faults can nucleate toward the upper surface of the subduction interface. At large depths within the interface,

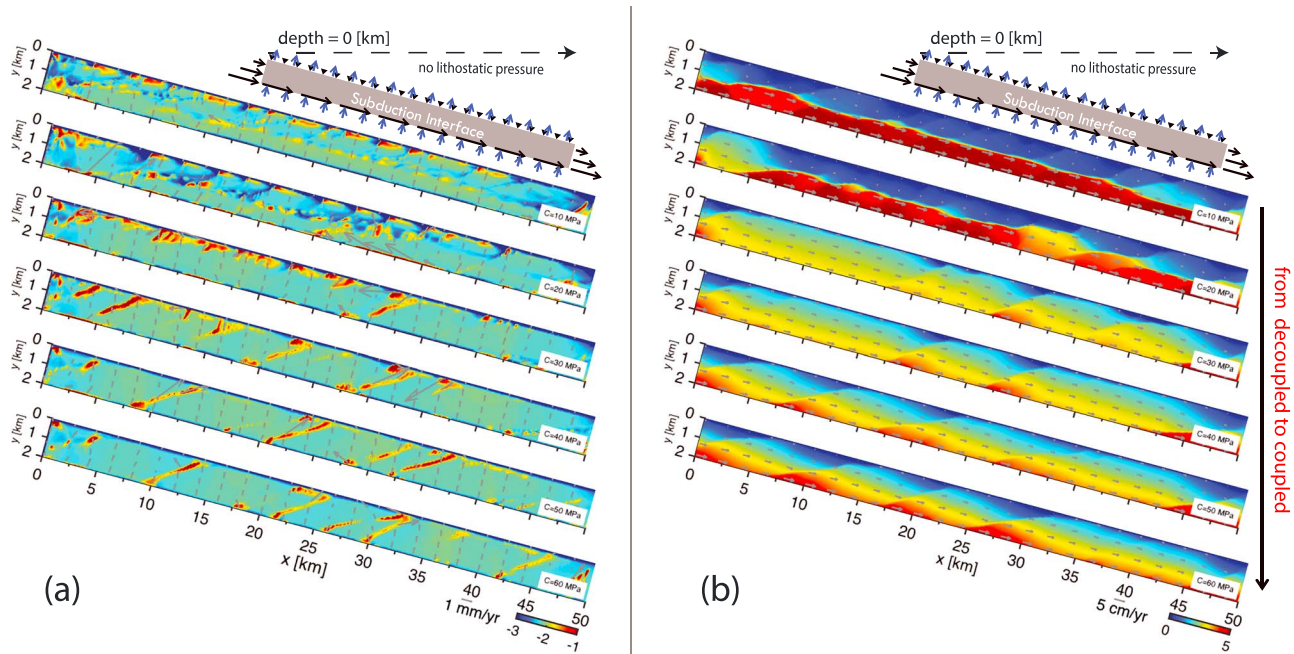


**Figure 3.** Influence of cohesion (cohesion increases from top to bottom): (a) porosity ( $\log_{10} \phi$ ) together with the Darcy velocity vectors and (b) x component of the solid velocity (color) together with solid velocity vectors. Refer to Figure 2 for porosity, solid, and Darcy velocity fields. The individual model results shown in both Figures 3a and 3b are associated with (from top to bottom) models M4, M7, M8, M9, M10, and M2.

the increased overburden pressure acts to close the pores/fractures, thereby inhibiting the generation of shear zones.

#### 4.5. Transition From Decoupled to Coupled Faulting Regime

There are two primary parameters, which determine the yield strength of the solid matrix at dry conditions, namely, the cohesion and the internal friction coefficient. The contribution to the yield strength from the cohesion is independent of the dynamics of the flow. This is in contrast to the contribution from the friction coefficient which is multiplied by  $P_{\text{eff}}$  (a dynamic quantity). Therefore, we investigate the influence of cohesion and internal friction coefficient in two series of experiments, in which we (i) fixed the friction coefficient to a value of 0.6 and varied the cohesion between 10 MPa and 60 MPa (models M4, M7, M8, M9, M10, and M2) and (ii) held cohesion constant at 60 MPa and varied the friction coefficient between 0.1 and 0.6 (models M12, M11, and M2).

Figure 3 shows the regimes of fluid activity and porosity (Figure 3a) and solid matrix deformation (Figure 3b) for different values of cohesion at 0.09 Myr. Figure 3b reveals that a gradual transition from the decoupled regime to the coupled regime occurs as the cohesion is increased from 10 MPa to 60 MPa. The transition is observed to occur for values of cohesion between 20 and 30 MPa. The transition is clearly apparent as the predominately subduction interface-parallel shear zone spanning the entire length of the model switches into a series of inclined regularly spaced shear bands, which crosscut the interface. In Figure 3a, a narrow discontinuous band of high porosity is observed to develop along the interface-parallel shear zone when the cohesion is  $< 20$  MPa. At higher values of cohesion ( $C = 40$ – $60$  MPa) a series of inclined high-porosity shear bands develop. With cohesion of 30 MPa, a transitional regime develops in which inclined shear bands coexist with a subduction interface-parallel high-porosity zone located close to the upper boundary.

Figure 4 shows the influences of varying the internal friction coefficient. The numerical results can be summarized as follows: (1) high-friction coefficient of the solid matrix (e.g.,  $\mu = 0.6$ ) produces a larger number of more steeply inclined high-porosity shear bands compared to models with low-friction coefficient (e.g.,  $\mu = 0.1$ ), which suggests that varying  $\mu$  has an effect to change the shear band angle; (2) due to the increased number of shear bands with larger values of  $\mu$ , the number of rigid blocks formed within the subduction interface also increases; and (3) while the fault orientation shows a tendency to rotate toward a plane parallel

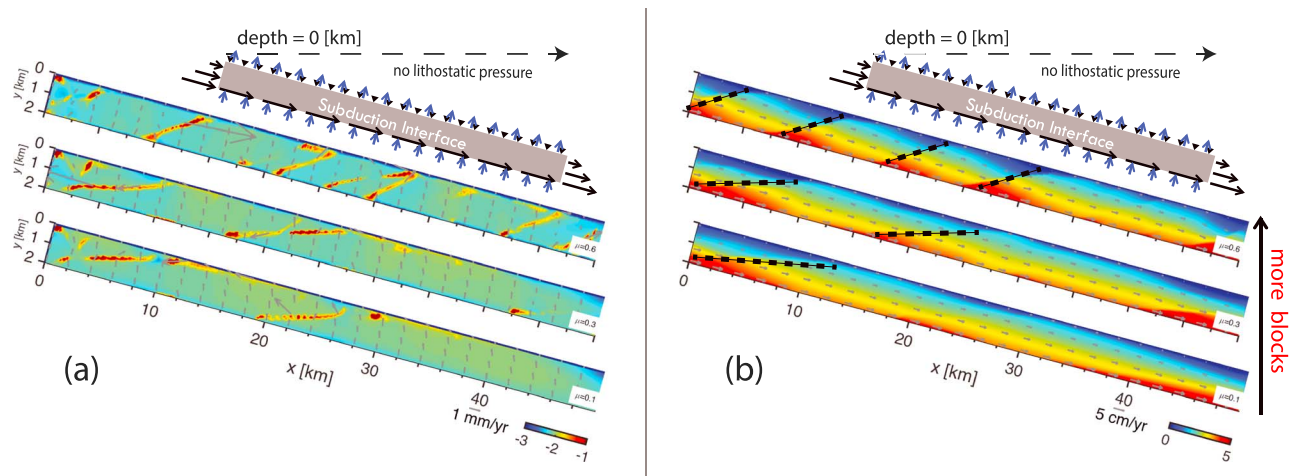


**Figure 4.** Influence of internal friction coefficient (friction coefficient decreases from top to bottom): (a) porosity ( $\log_{10}\phi$ ) together with the Darcy velocity vectors and (b)  $x$  component of the solid velocity together with solid velocity vectors. Refer to Figure 2 for porosity, solid, and Darcy velocity fields. Subfigures in Figures 4a and 4b from top to bottom represent the models of M2, M11, and M12.

to the subduction interface with decreasing friction coefficient, no obvious transition into the decoupled regime is observed.

In summary, both cohesion and internal friction coefficient notably affect the faulting pattern and spacing within the subduction interface. However, the transition from the coupled to the decoupled faulting regime is fundamentally governed by the magnitude of cohesion.

## 5. Discussion

In the previous sections, two possible faulting regimes that can occur within the subduction interface have been identified. Through a systematic parameter study, we conclude that it is the value of cohesion (tensile strength) of the solid matrix that controls the transition between the two regimes. In the following sections we analyze our numerical results and compare them with laboratory experiments and field observations. Additionally, we also discuss the limitations of our modeling study and propose some potential improvements for future numerical studies of the deforming subduction interface.

### 5.1. Porosity and Fluid Pressure Evolution

In Figure 5a we show volume-averaged porosity over time for models with different values of cohesion. The volume-averaged porosity seems to behave differently for the different faulting regimes: (1) for values of cohesion 10–20 MPa (decoupled regime), the temporal variation of the volume-averaged porosity is small, and the average porosity may evolve to values lower than the initial value; (2) when cohesion is 50–60 MPa (coupled regime) the volume-averaged porosity is observed to increase with time until it plateaus at approximately 0.03 Myr; and (3) for values of cohesion in the range of 30–40 MPa, the time required for the volume-averaged porosity to reach a maximum value is longer ( $\sim 0.06$  Myr). The maximum attained average porosity is generally larger than that obtained with models employing higher values of cohesion. We note, however, that we are studying a fully coupled, nonlinear system, so that the evolution of the average porosity is not linearly related to rheological parameters. For instance, regimes with  $C = 50$ , 60 MPa will produce lower porosity than regimes with  $C = 10$ , 20, but regimes with  $C = 30$ , 40 MPa will produce higher porosity.

Examination of the evolution of the volume-averaged fluid pressure over time (Figure 5b) shows the values rapidly increasing in the beginning of experiments ( $< 0.01$  Myr), then gradually decreasing. Models with high cohesion achieve higher peak fluid pressure, while models with low cohesion achieve a lower average peak fluid pressure. The average fluid pore pressure for models in the decoupled regime is lower than that observed in models in the coupled regime.

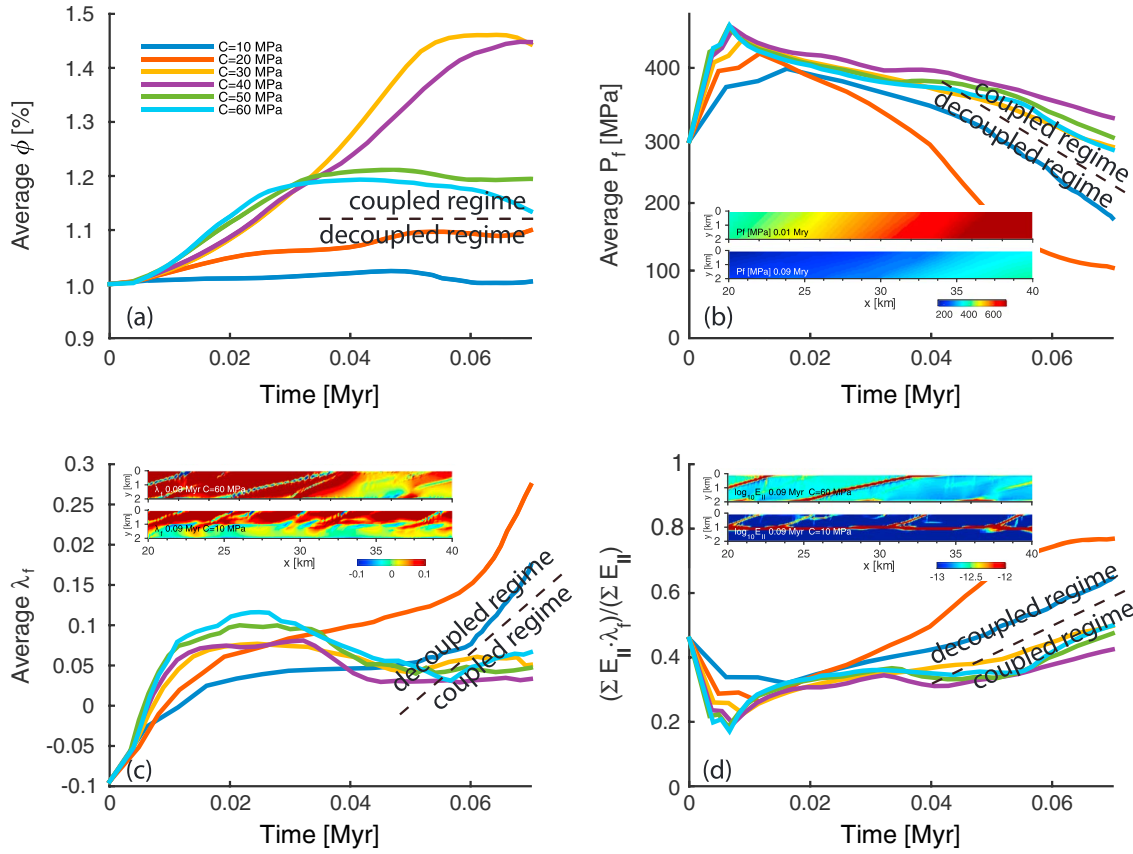


**Figure 5.** Temporal evolution of (a) volume-averaged porosity  $\phi$ ; (b) volume-averaged fluid pressure  $P_f$ , color plots show the fluid pressure  $P_f$  at 0.01 Myr (top inset) and 0.09 Myr (bottom inset); (c) volume-averaged fluid pressure factor  $\lambda_f$ , color plots show the fluid pressure factor  $\lambda_f$  using a high value of high cohesion ( $C = 60$  MPa, top inset) and a low value of cohesion ( $C = 10$  MPa, bottom inset); and (d) volume average of the fluid pressure factor normalized by the strain rate invariant  $\sum \dot{\epsilon}_{II} \lambda_f / \sum \dot{\epsilon}_{II}$ , color plots show the second invariant of the deviatoric strain rate  $\dot{\epsilon}_{II}$ .

The difference between the total pressure and fluid pressure plays an important role in defining the plastic strength of the solid matrix (equation (19)). A useful tool to analyze the effect of fluid pressure and total pressure on the rock strength is the effective friction  $\gamma'$  given by

$$\sigma_{\text{yield}} = C + \gamma(P - P_f) = C + \gamma'P. \quad (34)$$

We can then introduce a new variable, a fluid pressure factor, defined as the ratio of effective friction  $\gamma'$  and “dry” friction  $\gamma$  [Gerya and Meilick, 2011]:

$$\lambda_f = \frac{\gamma'}{\gamma} = 1 - \frac{P_f}{P} = \frac{(1 - \phi)(P_s - P_f)}{P}. \quad (35)$$

Figure 5c shows the volume-averaged  $\lambda_f$  evolution for models employing different values of cohesion.

From Figure 5c, the following observations are apparent: (1) for the first 0.02 Myr,  $\lambda_f$  increases rapidly in all experiments, indicating that the increasing/decreasing rate of total pressure is greater/smaller than the fluid pressure; (2) when the subduction interface is in the coupled regime, the fluid pressure factor is approximately constant for after 0.04 Myr, implying that the effective friction will also remain approximately constant; and (3) when the subduction interface is in the decoupled regime, the fluid pressure factor is observed to rapidly increase after 0.04 Myr. The increase in  $\lambda_f$  implies a simultaneous increase in the effective friction coefficient, indicating that the fluid pore pressure has a weaker effect on the decoupling mechanism. The inset within Figure 5c (color plots) provides a comparison of the spatial distribution of  $\lambda_f$  inside the subduction interface for the coupled (upper) and decoupled (lower) regimes. The coupled regime shows a



band of low values of  $\lambda_f$  ( $\lambda_f < 0$ ), reflecting a relatively high value for  $P_f$  or  $\varphi$ . In contrast, the decoupled regime has a zone of low  $\lambda_f$  ( $\lambda_f < 0$ ) within the upper layer and a zone of high  $\lambda_f$  ( $\lambda_f > 0$ ) in the lowermost layers.

According to the definition of the plastic rheology used (see equation (22)), the second invariant of the deviatoric strain rate  $\dot{\epsilon}_{II}$  can identify the position of shear zones along which most of the deformation occurs (see inset of Figure 5d). To examine the evolution of  $\lambda_f$  along such structures, we evaluated the strain rate-averaged value of  $\lambda_f$  given by  $\frac{\sum \dot{\epsilon}_{II} \lambda_f}{\sum \dot{\epsilon}_{II}}$ . The temporal evolution of this value is shown in Figure 5d. The strain rate-averaged  $\lambda_f$  is observed to decrease rapidly in the first  $\sim 0.075$  Myr, but afterward steadily increases. At the final stage of the model evolution, the strain rate-averaged  $\lambda_f$  is found to assume a larger value in the decoupled models.

## 5.2. Tectonic Overpressure and Underpressure

Figures 6a, 6c, 6e, and 6g compare the modeled total pressure, fluid pressure, and lithostatic pressure  $P_{lith} = \int_{z=0}^h \rho(z)g \, dz$ . The following observations can be summarized: (1) the coupled regime without the fluid-fluxed boundary condition (reference model M1; Figure 6a) generates tectonic overpressure [Gerya, 2015; Li et al., 2010] (i.e., the positive difference between the total and the lithostatic pressure) at all depths; (2) the decoupled regime without the fluid-fluxed boundary (model M3; Figure 6c) produces total pressures which are approximately equal to the lithostatic pressure for depths less than 15 km, and below 15 km depth produces small values of overpressure; (3) the coupled regime with the fluid-fluxed boundary (model M2; Figure 6e) shows a transition from overpressure to underpressure (i.e., the negative difference between the total and the lithostatic pressure) at  $\sim 5$  km depth; and (4) the decoupled regime with the fluid-fluxed boundary (model M4; Figure 6g) exhibits underpressure at all depths.

We can understand the causes of underpressure and overpressure and the transitions between them in the following way. Models with a high cohesion ( $C = 60$  MPa) result in an interface which is intrinsically stronger and thus leads to higher deviatoric stresses and overpressure (see Figures 6a and 6b). Models with a low cohesion ( $C = 10$  MPa) produce an interface, which is intrinsically weaker, thus producing smaller deviatoric stresses and near-lithostatic average pressure gradient (see Figures 6c and 6d). Introducing the fluid-fluxed boundary condition has similar effect for both coupled and decoupled models by systematically lowering pressure gradients along the entire subduction interface (see Figures 6f and 6h). The combination of a fluid-fluxed boundary, together with a low cohesion of rocks, thus leads to the most significant underpressure (see Figure 6g).

## 5.3. Comparison to Analogue Experiments and Natural Observations

Recent experimental studies on a semibrittle wet two-phase material suggest that fracture patterns arising from brittle deformation are controlled by the yield stress (YS): high YS produces tensile fracturing behavior, whereas low YS results in a confined shearing behavior. In Figure 7 we visually compare structures obtained from our models, exhibiting the coupled and decoupled deformation modes with the analogue experiments of Reber et al. [2015]. It is apparent that the coupled regime we observe is analogous to the experimental tensile fracturing pattern (refer to Figure 7b with Figure 7c), while our decoupled regime is akin to the experimental confined shearing pattern (refer to Figure 7f with Figure 7g). Compared to the analogue experiments, our numerical models are scaled to reflect subduction processes occurring at shallow and deep depths, and they consider a much longer subduction interface. In addition, our numerical models can also reconcile the fracture regimes in natural fluid/melt-bearing rocks, as demonstrated in Figure 7 [Reber et al., 2015].

Our numerical study also suggests that both coupled and decoupled regimes of fluid-assisted deformation and faulting could potentially exist within the subduction interface. The existence of the coupled regime is supported by observations at all scales, from micrometers to kilometers. Microscale experimental studies on the development of melt bands in partially molten aggregates [Holtzman et al., 2003a, 2003b; Katz et al., 2006; Kohlstedt and Holtzman, 2009] demonstrate regularly spaced inclined high-porosity microshear structures, which are similar to the structures observed in our subduction-interface experiments (refer to Figures 2a and 2b). Subduction interface fragmentation by larger-scale tectonic slicing [Bachmann et al., 2009; Ruh et al., 2015], together with the observed interface locking deformation mode [Moreno et al., 2010, 2014], also supports the existence of the coupled regime within natural subduction systems.



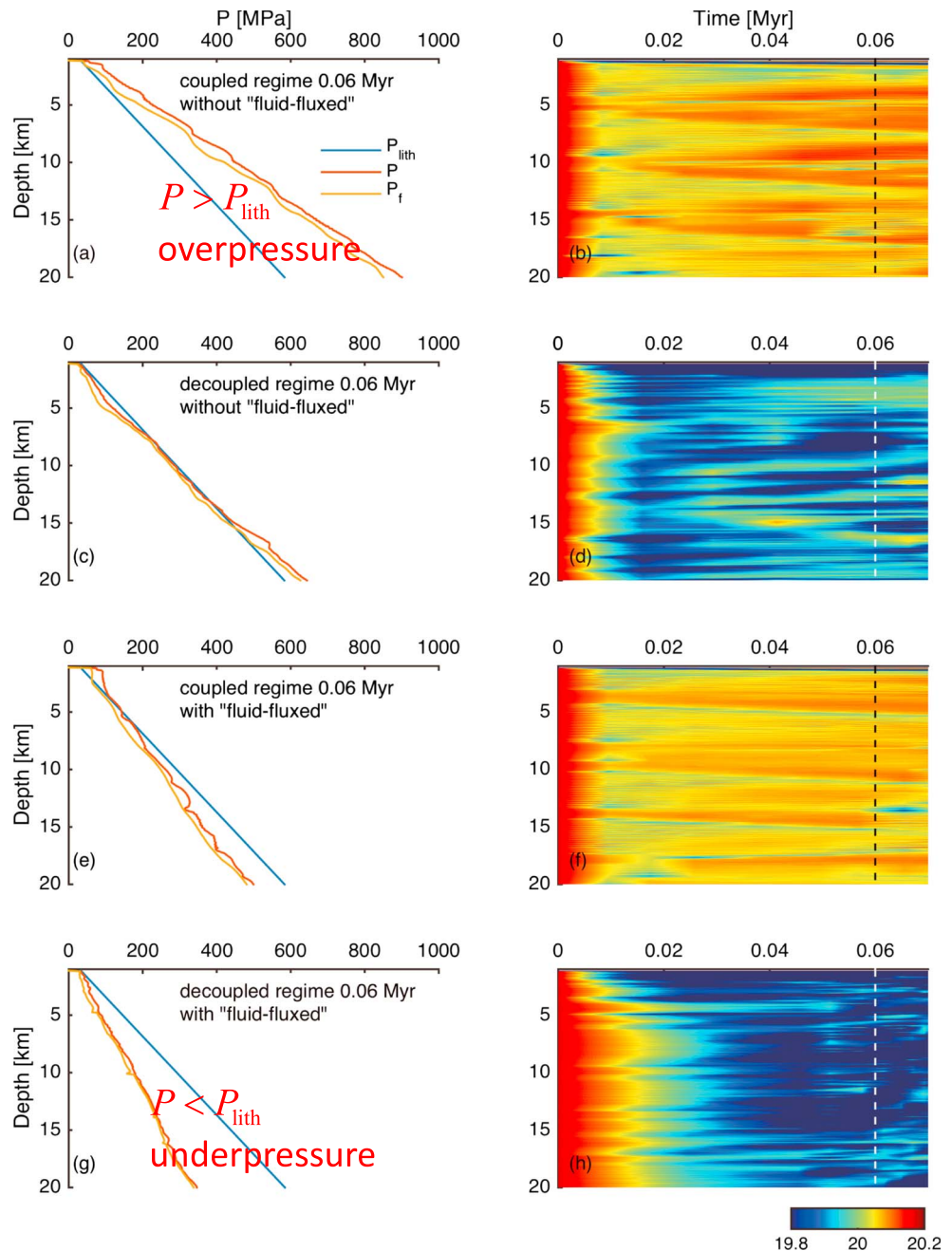


**Figure 6.** (a, c, e, and g) The averaged pressure versus depth (as measured from the surface of the Earth) at a time of 0.06 Myr, where  $P_{lith}$  is the lithostatic pressure,  $P$  is the total pressure, and  $P_f$  is the fluid pressure. (b, d, f, and h) The temporal evolution of the layer-averaged  $\log_{10} \gamma$ . The vertical dashed lines within each temporal evolution plot denote the time of 0.06 Myr. Figures 6a and 6b represent the models in the coupled regime without "fluid-fluxed" boundary. Figures 6c and 6d represent the models in the decoupled regime without fluid-fluxed boundary. Figures 6e and 6f represent the models in the coupled regime with fluid-fluxed boundary. Figures 6g and 6h represent the models in the decoupled regime with fluid-fluxed boundary.

The numerical results can also be considered in the context of larger-scale seismological observations of low-frequency earthquakes that are one manifestation of slow slip and ETS. Such phenomena occur at depths of 30–40 km in warm subduction zones, such as Nankai [Obara, 2002] and Cascadia [Rogers and Dragert, 2003], and represent deformation along the subduction zone interface at conditions that no longer support regular (e.g., brittle) earthquake behavior. A variety of evidence (e.g., seismic imaging of  $V_p/V_s$  ratios) [Shelly et al., 2006;

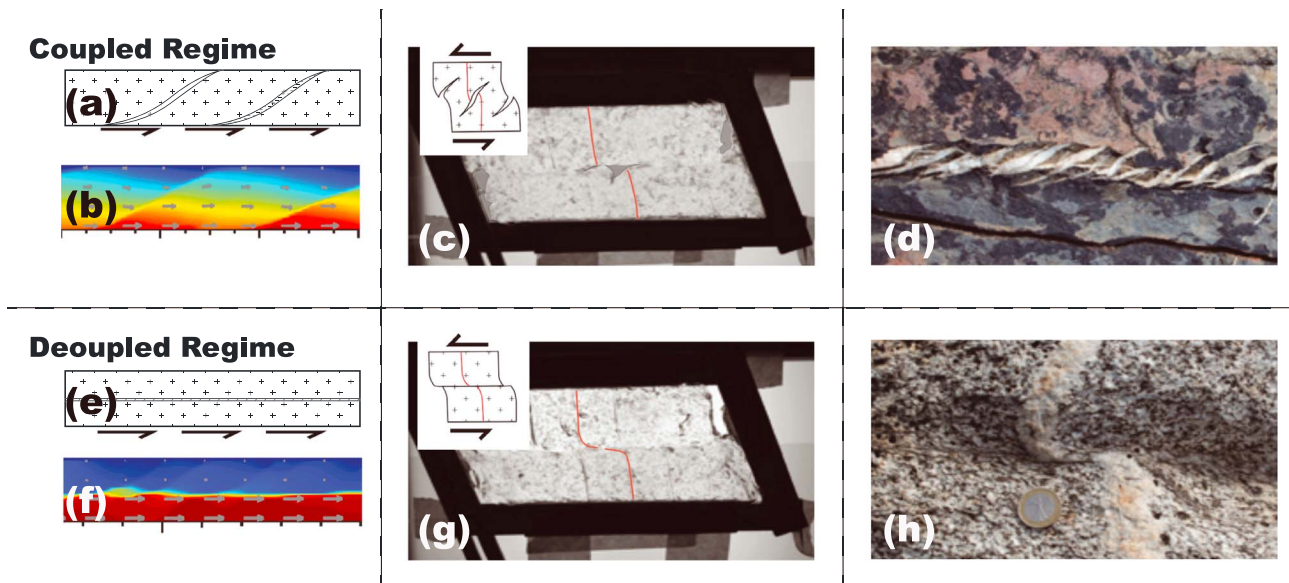


**Figure 7.** Comparison of our numerical experiments with analogue experiments and natural fractures in the field (modified after *Reber et al.* [2015]): (a) conceptual drawing of the coupled faulting regime, (b) coupled regime from numerical model M1 (subduction interface-parallel solid velocity component is shown), (c) coupled regime in analogue experiment, (d) coupled fracture in nature, (e) conceptual drawing of the decoupled regime, (f) decoupled regime from numerical model M4 (subduction interface-parallel solid velocity component is shown), (g) decoupled regime in analogue experiment, and (h) natural example of decoupled regime in nature.

*Peacock et al.*, 2011], triggering and modulation of tremor by tides and passing surface waves [*Rubinstein et al.*, 2007, 2008], suggests that ETS is enabled through near-zero effective stresses produced by high pore fluid pressure. Tremor is composed, at least in part, of many repeating low-frequency earthquakes that can be used to characterize the faulting within the interface at the scales on the order of 1 km. Well-defined, low-frequency earthquake focal mechanisms (e.g., southern Vancouver Island [*Royer and Bostock*, 2014]) indicate that faulting closely parallels to the plate boundary geometry, with little variability. This observation is consistent with the occurrence of slow-slip phenomena within a decoupled regime like that modeled here.

#### 5.4. Future Model Improvements

While our high-resolution subduction interface modeling reproduces structures consistent with some laboratory experiments and field observations through the self-consistent development of either a coupled or decoupled regime, these models are still highly simplified. From the perspective of the methodology and model design, some immediate improvements can be identified, which should be addressed in future work. These are summarized below:

1. Complex interface geometry: we note that in reality, the subduction interface is not just a uniformly long channel with parallel sides; rather, it is typically characterized by a more geometry complex domain (subduction channel) which is embedded between the subducted slab and the overriding plate and controlled by the distribution of rock density and viscosity along the subduction interface. Thus, thermomechanically self-consistent subduction interface geometries should be considered.
2. Thermal coupling: the effects of temperature on the buoyancy and rheology of subducted rocks were neglected in our models. Heat sources associated with radioactive decay were also ignored. Future hydro-thermo-mechanical [*Dymkova and Gerya*, 2013] models could, therefore, test influences of relevant thermal feedback.
3. Elasticity: our simplified models lack the short-term elastic deformation, which is an important attribute to be included within studies of subduction-related seismic phenomena, such as simulation of the seismic cycle and slow earthquake research [e.g., *van Dinther et al.*, 2014].
4. Compressibility: our two-phase flow model regarded both the solid phase and the fluid phase as incompressible materials. In most situations, this assumption is acceptable. However, geological materials,

especially in the presence of the fluid phase, are sensitive to volume change. For instance, when elasticity is included, the compressibility for two phases should not be ignored.

5. Chemical reactions: releasing or absorbing free fluid is relevant for subduction zones and will cause the imbalance of solid and fluid mass conservations. Thus, hydration/dehydration chemical reactions should be considered in the mass conservation equations.

All of the above mentioned improvements should be integrated in a fully coupled compressible hydro-thermo-mechanical-chemical model. Such methodologies (although applied for the condition of relatively small deformation of the solid matrix) have been widely utilized in safety assessment of geologic disposal systems for radioactive waste and spent nuclear fuel [Jing *et al.*, 1995; Rejeb and Cabrera, 2004]. The development of software to enable such simulations in the context of long-term, large-deformation geodynamic scenarios remains an ongoing research effort.

## 6. Conclusions

In this paper, we have investigated the shearing deformation-enhanced fluid migration and related faulting processes within the subduction interface. Based on a series of numerical experiments, the following conclusions can be made:

1. Shear deformation within the subduction interface triggers localized fluid migration along narrow bands of high porosity and high permeability.
2. Two end-member fracturing/faulting deformation modes are observed which we refer to as the coupled and decoupled regimes. The coupled regime is characterized by a subduction interface possessing a series of inclined, uniformly distributed shear bands, which separate the subduction interface into a series of rigid blocks. The decoupled regime is typified by the existence of a subduction interface-parallel main fault spanning the entire length of the interface and which effectively decouples a rigid stationary upper layer from a lower layer moving with the velocity of the subducting plate.
3. The depth of the subduction interface (mimicked via an imposed lithostatic pressure boundary condition) and the fluid-fluxed boundary condition adjust the location of shear bands in the coupled regime, as well as the location of the main fault within the interface in the decoupled regime.
4. The tensile strength (cohesion) of the solid matrix controls the deformation regime and pattern: low values of cohesion ( $C = 10$  MPa) lead to the decoupled regime, while high values of cohesion ( $C = 60$  MPa) lead to the coupled regime.
5. Increasing the friction coefficient decreases the spacing between the faults in the coupled regime and increases their inclination angle toward subduction interface parallel.
6. The simulated modes of deformation obtained from our numerical models are consistent with experimental studies and are supported by geological observations and geophysical data associated with subduction settings.

## Acknowledgments

We thank the discussions with Ylona van Dinther and Xiang Gao. This research is funded by ZIP project ([www.zip-itn.eu](http://www.zip-itn.eu)) in the People Programme (Marie Curie Actions) of the European Union's Seventh Framework Programme FP7/2007–2013 under REA grant agreement 604713. Data presented in this work are available upon request from the corresponding author.

## References

- Angiboust, S., T. Pettke, J. C. M. De Hoog, B. Caron, and O. Oncken (2014), Channelized fluid flow and eclogite-facies metasomatism along the subduction shear zone, *J. Petrol.*, *55*, 883–916, doi:10.1093/petrology/egu010.
- Arcay, D., E. Tric, and M.-P. Doin (2005), Numerical simulations of subduction zones: Effect of slab dehydration on the mantle wedge dynamics, *Phys. Earth Planet. Int.*, *149*(1), 133–153.
- Austrheim, H. (1987), Eclogitization of lower crustal granulites by fluid migration through shear zones, *Earth Planet. Sci. Lett.*, *81*, 221–232, doi:10.1016/0012-821X(87)90158-0.
- Bachmann, R., O. Oncken, J. Glodny, W. Seifert, V. Georgieva, and M. Sudo (2009), Exposed plate interface in the European Alps reveals fabric styles and gradients related to an ancient seismogenic coupling zone, *J. Geophys. Res.*, *114*, B05402, doi:10.1029/2008JB005927.
- Beroza, G. C., and S. Ide (2011), Slow earthquakes and nonvolcanic tremor, *Annu. Rev. Earth Planet. Sci.*, *39*, 271–296.
- Bostock, M. G. (2013), The Moho in subduction zones, *Tectonophysics*, *609*, 547–557, doi:10.1016/j.tecto.2012.07.007.
- Brown, J. R., G. C. Beroza, S. Ide, K. Ohta, D. R. Shelly, S. Y. Schwartz, W. Rabbel, M. Thorwart, and H. Kao (2009), Deep low-frequency earthquakes in tremor localize to the plate interface in multiple subduction zones, *Geophys. Res. Lett.*, *36*, L19306, doi:10.1029/2009GL040027.
- Cagnioncle, A. M., E. Parmentier, and L. T. Elkins-Tanton (2007), Effect of solid flow above a subducting slab on water distribution and melting at convergent plate boundaries, *J. Geophys. Res.*, *112*, B09402, doi:10.1029/2007JB004934.
- Christensen, N. I. (1996), Poisson's ratio and crustal seismology, *J. Geophys. Res.*, *101*, 3139–3156, doi:10.1029/95JB03446.
- Connolly, J. A. D., and Y. Y. Podladchikov (1998), Compaction-driven fluid flow in viscoelastic rock, *Geodin. Acta*, *11*(2), 55–84.
- Cox, S. F. (1995), Faulting processes at high fluid pressures: An example of fault valve behavior from the Wattle Gully Fault, Victoria, Australia, *J. Geophys. Res.*, *100*, 12,841–12,859, doi:10.1029/95JB00915.
- Duarte, J. C., W. P. Schellart, and A. R. Cruden (2015), How weak is the subduction zone interface?, *Geophys. Res. Lett.*, *42*, 2664–2673, doi:10.1002/2014GL062876.

- Dymkova, D. (2014), Numerical modelling of coupled thermo-mechanical and fluid transport process at convergent margins.
- Dymkova, D., and T. V. Gerya (2013), Porous fluid flow enables oceanic subduction initiation on Earth, *Geophys. Res. Lett.*, **40**, 5671–5676, doi:10.1002/2013GL057798.
- Faccenda, M. (2014), Water in the slab: A trilogy, *Tectonophysics*, **614**, 1–30, doi:10.1016/j.tecto.2013.12.020.
- Faccenda, M., T. V. Gerya, and L. Burlini (2009), Deep slab hydration induced by bending-related variations in tectonic pressure, *Nat. Geosci.*, **2**(11), 790–793, doi:10.1038/ngeo656.
- Faccenda, M., T. V. Gerya, N. S. Mancktelow, and L. Moresi (2012), Fluid flow during slab unbending and dehydration: Implications for intermediate-depth seismicity, slab weakening and deep water recycling, *Geochem. Geophys. Geosyst.*, **13**, Q01010, doi:10.1029/2011GC003860.
- Fowler, A. C. (1990a), A compaction model for melt transport in the Earth's asthenosphere, Part II: Applications, in *Magma Transport and Storage*, edited by M. P. Ryan, pp. 15–32, John Wiley, New York.
- Fowler, A. C. (1990b), A compaction model for melt transport in the Earth's asthenosphere. Part I: The basic model, in *Magma Transport and Storage*, edited by M. P. Ryan, pp. 3–14, John Wiley, New York.
- Gerya, T. V. (2011), Future directions in subduction modeling, *J. Geodyn.*, **52**(5), 344–378.
- Gerya, T. V. (2015), Tectonic overpressure and underpressure in lithospheric tectonics and metamorphism, *J. Metamorph. Geol.*, **33**(8), 785–800.
- Gerya, T. V., and F. Meilick (2011), Geodynamic regimes of subduction under an active margin: Effects of rheological weakening by fluids and melts, *J. Metamorph. Geol.*, **29**(1), 7–31.
- Gerya, T. V., and D. A. Yuen (2003), Rayleigh–Taylor instabilities from hydration and melting propel “cold plumes” at subduction zones, *Earth Planet. Sci. Lett.*, **212**(1), 47–62.
- Gerya, T. V., B. Stöckhert, and A. L. Perchuk (2002), Exhumation of high-pressure metamorphic rocks in a subduction channel: A numerical simulation, *Tectonics*, **21**(6), 1056, doi:10.1029/2002TC001406.
- Gerya, T. V., J. A. Connolly, D. A. Yuen, W. Gorczyk, and A. M. Capel (2006), Seismic implications of mantle wedge plumes, *Phys. Earth Planet. Inter.*, **156**(1), 59–74.
- Gerya, T. V., L. Perchuk, and J.-P. Burg (2008), Transient hot channels: Perpetrating and regurgitating ultrahigh-pressure, high-temperature crust–mantle associations in collision belts, *Lithos*, **103**(1), 236–256.
- Gomberg, J. (2010), Slow-slip phenomena in Cascadia from 2007 and beyond: A review, *Geol. Soc. Am. Bull.*, **122**(7–8), 963–978.
- Grevenmeyer, I., C. R. Ranero, E. R. Flueh, D. Kläschen, and J. Bialas (2007), Passive and active seismological study of bending-related faulting and mantle serpentinization at the Middle America trench, *Earth Planet. Sci. Lett.*, **258**(3–4), 528–542, doi:10.1016/j.epsl.2007.04.013.
- Gueguen, Y., and J. Dienes (1989), Transport properties of rocks from statistics and percolation, *Math. Geol.*, **21**(1), 1–13.
- Hacker, B. R., S. M. Peacock, G. A. Abers, and S. D. Holloway (2003), Subduction factory 2. Are intermediate-depth earthquakes in subducting slabs linked to metamorphic dehydration reactions?, *J. Geophys. Res.*, **108**(B1), 2030, doi:10.1029/2001JB001129.
- Hebert, L. B., P. Antoshechkina, P. Asimow, and M. Gurnis (2009), Emergence of a low-viscosity channel in subduction zones through the coupling of mantle flow and thermodynamics, *Earth Planet. Sci. Lett.*, **278**(3), 243–256.
- Holtzman, B. K., N. J. Groebner, M. E. Zimmerman, S. B. Ginsberg, and D. L. Kohlstedt (2003b), Stress-driven melt segregation in partially molten rocks, *Geochem. Geophys. Geosyst.*, **4**(5), 8607, doi:10.1029/2001GC000258.
- Holtzman, B., D. Kohlstedt, M. Zimmerman, F. Heidelbach, T. Hiraga, and J. Hustoft (2003a), Melt segregation and strain partitioning: Implications for seismic anisotropy and mantle flow, *Science*, **301**(5637), 1227–1230.
- Iwamori, H. (1998), Transportation of H<sub>2</sub>O and melting in subduction zones, *Earth Planet. Sci. Lett.*, **160**(1), 65–80.
- Iwamori, H. (2000), Deep subduction of H<sub>2</sub>O and deflection of volcanic chain toward backarc near triple junction due to lower temperature, *Earth Planet. Sci. Lett.*, **181**(1), 41–46.
- Iwamori, H. (2004), Phase relations of peridotites under H<sub>2</sub>O-saturated conditions and ability of subducting plates for transportation of H<sub>2</sub>O, *Earth Planet. Sci. Lett.*, **227**(1), 57–71.
- Iwamori, H. (2007), Transportation of H<sub>2</sub>O beneath the Japan arcs and its implications for global water circulation, *Chem. Geol.*, **239**(3), 182–198.
- Iwamori, H., and T. Nakakuki (2013), Fluid processes in subduction zones and water transport to the deep mantle, *Phys. Chem. Deep Earth*, **372**–391.
- Jing, L., C.-F. Tsang, and O. Stephansson (1995), DECOVALEX—An international co-operative research project on mathematical models of coupled THM processes for safety analysis of radioactive waste repositories, *Int. J. Rock Mech. Min. Sci. Geomech. Abstr.*, **32**, 389–398.
- Katz, R. F., M. Spiegelman, and B. Holtzman (2006), The dynamics of melt and shear localization in partially molten aggregates, *Nature*, **442**(7103), 676–679, doi:10.1038/nature05039.
- Keller, T., D. A. May, and B. J. Kaus (2013), Numerical modelling of magma dynamics coupled to tectonic deformation of lithosphere and crust, *Geophys. J. Int.*, **195**(3), 1406–1442.
- Kohlstedt, D. L., and B. K. Holtzman (2009), Shearing melt out of the Earth: An experimentalist's perspective on the influence of deformation on melt extraction, *Annu. Rev. Earth Planet. Sci.*, **37**, 561–593.
- Li, Z., T. V. Gerya, and J. P. Burg (2010), Influence of tectonic overpressure on P–T paths of HP–UHP rocks in continental collision zones: Thermomechanical modelling, *J. Metamorph. Geol.*, **28**(3), 227–247.
- McKenzie, D. (1984), The generation and compaction of partially molten rock, *J. Petrol.*, **25**(3), 713–765.
- Morency, C., R. S. Huisman, C. Beaumont, and P. Fullsack (2007), A numerical model for coupled fluid flow and matrix deformation with applications to disequilibrium compaction and delta stability, *J. Geophys. Res.*, **112**, B10407, doi:10.1029/2006JB004701.
- Moreno, M., M. Rosenau, and O. Oncken (2010), 2010 Maule earthquake slip correlates with pre-seismic locking of Andean subduction zone, *Nature*, **467**(7312), 198–202.
- Moreno, M., C. Haberland, O. Oncken, A. Rietbrock, S. Angiboust, and O. Heidbach (2014), Locking of the Chile subduction zone controlled by fluid pressure before the 2010 earthquake, *Nat. Geosci.*, **7**(4), 292–296, doi:10.1038/NGEO2102.
- Obara, K. (2002), Nonvolcanic deep tremor associated with subduction in southwest Japan, *Science*, **296**(5573), 1679–1681.
- Peacock, S. M. (1990), Fluid processes in subduction zones, *Science*, **248**(4953), 329–337.
- Peacock, S. M., N. I. Christensen, M. G. Bostock, and P. Audet (2011), High pore pressures and porosity at 35 km depth in the Cascadia subduction zone, *Geology*, **39**(5), 471–474, doi:10.1130/G31649.1.
- Ranalli, G. (1995), *Rheology of the Earth*, pp. 102–103, Chapman and Hall, London.
- Ranero, C. R., J. P. Morgan, K. McIntosh, and C. Reichert (2003), Bending-related faulting and mantle serpentinization at the Middle America trench, *Nature*, **425**(6956), 367–373, doi:10.1038/nature01961.
- Ranero, C., and V. Sallares (2004), Geophysical evidence for hydration of the crust and mantle of the Nazca plate during bending at the north Chile trench, *Geology*, **32**(7), 549–552.



- Reber, J. E., L. L. Lavier, and N. W. Hayman (2015), Experimental demonstration of a semi-brittle origin for crustal strain transients, *Nat. Geosci.*, **8**(9), 712–715.
- Rejeb, A., and J. Cabrera (2004), DECOVALEX-THMC, description for task C, excavation disturbed zone (EDZ) in the argillaceous Tournemire site (France) *Rep Tech. Rep.*, Institute of Radioprotection and Nuclear Safety (IRSN), France.
- Richard, G., D. Bercovici, and S.-I. Karato (2006), Slab dehydration in the Earth's mantle transition zone, *Earth Planet. Sci. Lett.*, **251**(1), 156–167.
- Richard, G. C., and D. Bercovici (2009), Water-induced convection in the Earth's mantle transition zone, *J. Geophys. Res.*, **114**, B01205, doi:10.1029/2008JB005734.
- Rogers, G., and H. Dragert (2003), Episodic tremor and slip on the Cascadia subduction zone: The chatter of silent slip, *Science*, **300**(5627), 1942–1943.
- Royer, A., and M. Bostock (2014), A comparative study of low frequency earthquake templates in northern Cascadia, *Earth Planet. Sci. Lett.*, **402**, 247–256.
- Rozhko, A. Y., Y. Y. Podladchikov, and F. Renard (2007), Failure patterns caused by localized rise in pore-fluid overpressure and effective strength of rocks, *Geophys. Res. Lett.*, **34**, L22304, doi:10.1029/2007GL031696.
- Rubinstein, J. L., J. E. Vidale, J. Gombert, P. Bodin, K. C. Creager, and S. D. Malone (2007), Non-volcanic tremor driven by large transient shear stresses, *Nature*, **448**(7153), 579–582.
- Rubinstein, J. L., M. La Rocca, J. E. Vidale, K. C. Creager, and A. G. Wech (2008), Tidal modulation of nonvolcanic tremor, *Science*, **319**(5860), 186–189.
- Ruh, J., L. Le Pourhiet, P. Agard, E. Burov, and T. V. Gerya (2015), Tectonic slicing of subducting oceanic crust along plate interfaces: Numerical modeling, *Geochem. Geophys. Geosyst.*, **16**, 3505–3531, doi:10.1002/2015GC005998.
- Saffer, D. M., and H. J. Tobin (2011), Hydrogeology and mechanics of subduction zone forearcs: Fluid flow and pore pressure, *Annu. Rev. Earth Planet. Sci.*, **39**, 157–186, doi:10.1146/annurev-earth-040610-133408.
- Shelly, D. R., G. C. Beroza, S. Ide, and S. Nakamura (2006), Low-frequency earthquakes in Shikoku, Japan and their relationship to episodic tremor and slip, *Nature*, **442**, 188–191, doi:10.1038/nature04931.
- Shimojo, K., B. Enescu, Y. Yagi, and T. Takeda (2014), Fluid-driven seismicity activation in northern Nagano region after the 2011 M9.0 Tohoku-oki earthquake, *Geophys. Res. Lett.*, **41**, 7524–7531, doi:10.1002/2014GL061763.
- Sibson, R. H. (1994), Crustal stress, faulting and fluid flow, *Geol. Soc. London, Spec. Publ.*, **78**, 69–84, doi:10.1144/GSL.SP.1994.078.01.07.
- Sibson, R. H. (1996), Structural permeability of fluid-driven fault-fracture meshes, *J. Struct. Geol.*, **18**, 1031–1042, doi:10.1016/0191-8141(96)00032-6.
- Sibson, R. H., and J. Scott (1998), Stress/fault controls on the containment and release of overpressured fluids: Examples from gold-quartz vein systems in Juneau, Alaska; Victoria, Australia and Otago, New Zealand, *Ore Geol. Rev.*, **13**, 293–306, doi:10.1016/S0169-1368(97)00023-1.
- Soyer, W., and M. Unsworth (2006), Deep electrical structure of the northern Cascadia (British Columbia, Canada) subduction zone: Implications for the distribution of fluids, *Geology*, **34**, 53–56, doi:10.1130/G21951.1.
- Stevenson, D. J., and D. R. Scott (1991), Mechanics of fluid-rock systems, *Annu. Rev. Fluid Mech.*, **23**(1), 305–339.
- van Dinther, Y., P. M. Mai, L. Dalguer, and T. V. Gerya (2014), Modeling the seismic cycle in subduction zones: The role and spatiotemporal occurrence of off-megathrust earthquakes, *Geophys. Res. Lett.*, **41**, 1194–1201, doi:10.1002/2013GL058886.
- Wada, I., K. Wang, J. He, and R. D. Hyndman (2008), Weakening of the subduction interface and its effects on surface heat flow, slab dehydration, and mantle wedge serpentinization, *J. Geophys. Res.*, **113**, B04402, doi:10.1029/2007JB005190.
- Wang, D., M. Mookherjee, Y. Xu, and S.-i. Karato (2006a), The effect of water on the electrical conductivity of olivine, *Nature*, **443**(7114), 977–980.
- Wang, K., J. He, and Y. Hu (2006b), A note on pore fluid pressure ratios in the Coulomb wedge theory, *Geophys. Res. Lett.*, **33**, L19310, doi:10.1029/2006GL027233.
- Weinberg, R. F., and K. Regenauer-Lieb (2010), Ductile fractures and magma migration from source, *Geology*, **38**, 363–366, doi:10.1130/G30482.1.
- Wilson, C. R., M. Spiegelman, P. E. van Keken, and B. R. Hacker (2014), Fluid flow in subduction zones: The role of solid rheology and compaction pressure, *Earth Planet. Sci. Lett.*, **401**, 261–274.
- Zhu, G., T. V. Gerya, D. A. Yuen, S. Honda, T. Yoshida, and J. A. Connolly (2009), Three-dimensional dynamics of hydrous thermal-chemical plumes in oceanic subduction zones, *Geochem. Geophys. Geosyst.*, **10**, Q11006, doi:10.1029/2009GC002625.